

Single electrons on solid neon as a solid-state qubit platform

<https://doi.org/10.1038/s41586-022-04539-x>

Received: 10 August 2021

Accepted: 9 February 2022

Published online: 4 May 2022

 Check for updates

Xianjing Zhou¹, Gerwin Koolstra², Xufeng Zhang¹, Ge Yang^{3,4}, Xu Han¹, Brennan Dizdar⁵, Xinhao Li¹, Ralu Divan¹, Wei Guo^{6,7}, Kater W. Murch⁸✉, David I. Schuster^{5,9} & Dafei Jin¹✉

Progress towards the realization of quantum computers requires persistent advances in their constituent building blocks—qubits. Novel qubit platforms that simultaneously embody long coherence, fast operation and large scalability offer compelling advantages in the construction of quantum computers and many other quantum information systems^{1–3}. Electrons, ubiquitous elementary particles of non-zero charge, spin and mass, have commonly been perceived as paradigmatic local quantum information carriers. Despite superior controllability and configurability, their practical performance as qubits through either motional or spin states depends critically on their material environment^{3–5}. Here we report our experimental realization of a qubit platform based on isolated single electrons trapped on an ultraclean solid neon surface in vacuum^{6–13}. By integrating an electron trap in a circuit quantum electrodynamics architecture^{14–20}, we achieve strong coupling between the motional states of a single electron and a single microwave photon in an on-chip superconducting resonator. Qubit gate operations and dispersive readout are implemented to measure the energy relaxation time T_1 of 15 μ s and phase coherence time T_2 over 200 ns. These results indicate that the electron-on-solid-neon qubit already performs near the state of the art for a charge qubit²¹.

The rapid growth of quantum information science and technology in recent years has accompanied the remarkable success of various qubit platforms in various domains of quantum information processing. Notable examples include superconducting quantum circuits^{14,15,22–25}, semiconductor quantum dots^{26–31}, electromagnetically trapped ions^{32–36}, optically trapped atoms^{37–40}, natural or implanted defects^{41–44}, and magnetic molecules^{45–48}. Among different quantum information carriers, isolated single electrons—paradigmatic charged spin- $\frac{1}{2}$ massive particles that naturally interact with photons through quantum electrodynamics (QED)—offer conceivably the straightest approach for efficient manipulation and remote entanglement. So far, electron qubits have been made predominantly in semiconductor heterojunctions and semiconductor–oxide interfaces^{3–5}. Despite standardized device fabrication and convenient electrical control, a major challenge faced by these electron qubits is the limited coherence time due to material imperfections or background noise^{3–5}. In this circumstance, a new type of single-electron qubit, embedded in a low-noise pure environment, may open up unprecedented opportunities to resolve the coherence challenge. Along with the inherent features of fast operation and large scalability, this single-electron qubit platform holds great potential for development into an ideal quantum computing architecture in the future.

In this work, we demonstrate a solid-state single-electron qubit platform based on trapping and manipulating isolated single electrons on an ultraclean solid neon surface in vacuum. By integrating the electron trap in a hybrid circuit QED architecture^{14–20}, we observe vacuum Rabi splitting between the motional states of a single electron and a single microwave photon in an on-chip superconducting resonator. This observation lays the foundation for the quantum coherent control and (single-shot) dispersive readout of electron charge (motional-state) qubits at microwave frequencies in this system. By detuning the electron transition frequency with respect to the resonator frequency, we perform complete qubit characterization, that is, two-tone qubit spectroscopy⁴⁹ and time-domain measurements⁵⁰, including Rabi oscillations, T_1 energy relaxation time and T_2 phase coherence time measurements. Without optimization, the measured $T_1 = 15 \mu\text{s}$ and $T_2 \gtrsim 200 \text{ ns}$ have already reached the state of the art for a charge qubit²¹, highlighting the promise of this new material environment. With projected development using spin-charge conversion^{16,27}, we anticipate the nearly perfect spinless environment formed by solid neon (the naturally occurring 0.27% abundance of spinful ^{21}Ne can be easily purified away) to support electron spin qubits with an estimated coherence time of over 1 s (refs. ^{12,16,19,51}). Beyond quantum computing, this solid-state single-electron qubit platform creates an appealing hybrid quantum

¹Center for Nanoscale Materials, Argonne National Laboratory, Lemont, IL, USA. ²Computational Research Division, Lawrence Berkeley National Laboratory, Berkeley, CA, USA. ³The NSF AI Institute for Artificial Intelligence and Fundamental Interactions, Cambridge, USA. ⁴Computer Science and Artificial Intelligence Laboratory, Massachusetts Institute of Technology, Cambridge, MA, USA. ⁵James Franck Institute and Department of Physics, University of Chicago, Chicago, IL, USA. ⁶National High Magnetic Field Laboratory, Tallahassee, FL, USA. ⁷Department of Mechanical Engineering, FAMU-FSU College of Engineering, Florida State University, Tallahassee, FL, USA. ⁸Department of Physics, Washington University in St. Louis, St. Louis, MO, USA. ⁹Pritzker School of Molecular Engineering, University of Chicago, Chicago, IL, USA. ✉e-mail: murch@physics.wustl.edu; djin@anl.gov

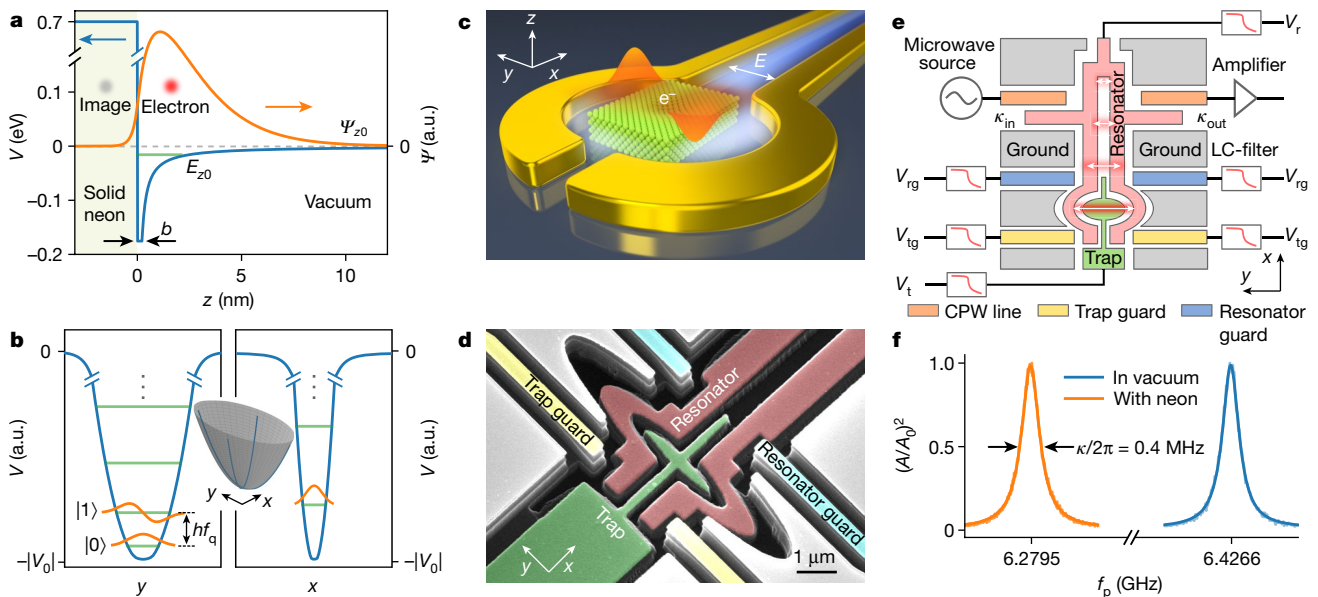


Fig. 1 | Electronic structure and device design of the single-electron circuit QED architecture on solid neon.

a, Potential energy seen by an excess electron approaching a flat solid neon surface and calculated ground-state eigenenergy and wavefunction in the z motion. **b**, Schematic of in-plane trapping potential that defines the motional state qubit in the y direction. **c**, Conceptual illustration of a single electron trapped on a solid neon surface and interacting with microwave photons at the open end of a superconducting coplanar stripline resonator. The electric dipole transition and the electric field of microwave photons are aligned in the y direction. **d**, (False-color) scanning electron microscopy picture of the fabricated device around the electron trap and photon coupling region. The trap and two striplines reside inside an etched channel that is $3.5\text{ }\mu\text{m}$ wide and $1.5\text{ }\mu\text{m}$ deep. **e**, Specific device

structure and functionalities of different components. The superconducting quarter-wavelength double-stripline resonator is measured in transmission by the input and output through coplanar waveguides (CPWs) with coupling rates of κ_{in} and κ_{out} , respectively. The antisymmetric mode has its electric field maximum at the open end and the field direction as indicated by the arrows. The resonator is biased with a d.c. voltage of V_r to control the number of electrons in the reservoir. Three additional d.c. electrodes (trap, trap guard and resonator guard), biased with the voltages V_t , V_{tg} and V_{rg} , control the single-electron trapping and frequency detuning. Each electrode has its own on-chip low-pass LC filter. **f**, Measured resonance peaks before ($f_r = 6.4266\text{ GHz}$) and after ($f_r = 6.2795\text{ GHz}$) neon fully fills the channel, showing the fitted resonator linewidth $\kappa/2\pi = 0.4\text{ MHz}$. a.u., arbitrary units.

framework that can connect various qubit platforms, thereby paving new pathways in quantum information science and technology.

Electronic structure and device design

Neon (Ne) is a noble-gas element next to helium (He) in the periodic table. By contrast to He, which is a liquid (superfluid) even at zero temperature, unless a large pressure of at least 25 bar is applied, Ne spontaneously turns into a face-centred-cubic crystal after passing its triple point at the elevated temperature $T_t = 24.556\text{ K}$ and moderate pressure $P_t = 0.43\text{ bar}$ (refs. ^{52–54}). At near-zero temperature, solid Ne can form a free surface to vacuum and serve as an ultraclean substrate with no uncontrollable impurities or electromagnetic noise^{55,56}.

When an excess electron approaches a semi-infinite solid Ne surface at $z = 0$ from vacuum, two effects lead to an out-of-plane trapping potential that can bind the electron to the surface (Fig. 1a). A repulsive barrier of constant potential about 0.7 eV occurs due to the Pauli exclusion between the excess electron and atomic shell electrons. In addition, an attractive polarization potential, $V(z) = -(\epsilon - 1)/[(\epsilon + 1)e^2/4z]$, ($z > b$), with a dielectric constant $\epsilon = 1.244$ and short-range cutoff $b \approx 2.3\text{ \AA}$, occurs because of the induced image charge inside solid Ne^{6,7,19}. With this potential, the electron's z motion has a ground-state energy $E_{z0} = -15.8\text{ meV}$ and an eigen-wavefunction peaked at a distance of about 1 nm from the surface (Fig. 1a). The energy cost to bring the electron to the first excited state in z is 12.7 meV , which is equivalent to a 147 K activation temperature. Therefore, at our 10 mK experimental temperature, the electron's motion is frozen within the subband of ground state in z . Previous studies have verified that a solid Ne surface can hold a non-degenerate two-dimensional electron gas with a high density of approximately 10^{10} cm^{-2} and a high mobility of approximately $10^4\text{ cm}^2\text{ V}^{-1}\text{ s}^{-1}$ (ref. ⁵⁷).

Condensed (liquid or solid) noble-gas elements with positive (repulsive) electron affinity are the only materials in nature that can hold electrons on a free surface in vacuum. Practically, all other materials, even those that are electronically insulating and atomically smooth, have negative (attractive) electron affinity and contain charged contaminants or dangling bonds on the surface that can capture and localize excess electrons at atomic to molecular scales^{58,59}. Although the electron-on-solid-Ne (eNe) system can be considered conceptually as an extension to the historically more studied electron-on-liquid-He (eHe) system, it exhibits much stronger surface rigidity that suppresses decoherence through surface excitations^{16–18}. Compared with eHe that was proposed as a qubit platform over two decades ago^{9,11–13,16–18}, eNe embodies a potentially transformative solid-state qubit platform^{10,19,55}.

On a flat Ne surface, the electron takes plane-wave eigenstates in the xy plane. To confine the electron in the plane, we use carefully designed lateral trapping electrodes to hold the electrons individually and deterministically in space¹⁸, with a trapping time exceeding two months. We tune the electrode voltages to further constrain the electron's x motion to its ground state and take the two lowest energy states of y motion as the qubit states (Fig. 1b). Figure 1c shows a simplified conceptual illustration of our arrangement of the trapped electron and microwave resonator. The electron is on the solid Ne surface at the open end (in a 'clamp' shape) of a quarter-wavelength coplanar double-stripline resonator, which carries a symmetric and an antisymmetric mode^{18,60}. Both modes have the electric field maximum at the open end, but only the antisymmetric mode has the field direction aligned with electron's motion in y . Figure 1d displays a scanning electron microscopy image of the actual device structure around the trapping area. All the metal lines and ground planes are made of superconducting niobium (Nb) deposited on a high-resistivity silicon substrate. A 'trap' electrode,

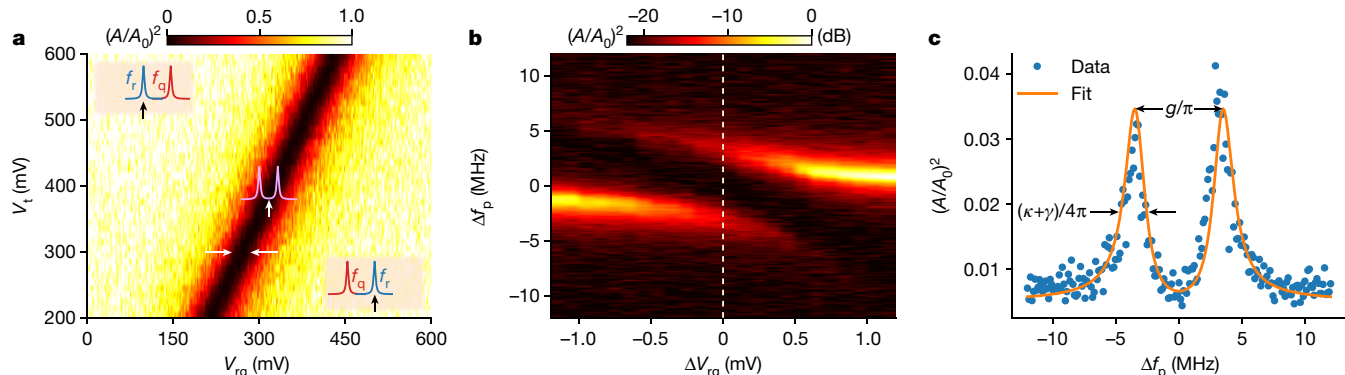


Fig. 2 | Strong coupling and vacuum Rabi splitting between a single electron on solid neon and a single microwave photon in a superconducting resonator. **a**, Normalized microwave transmission amplitude $(A/A_0)^2$ probed at the resonator frequency f_r (black and white vertical arrows in the insets) versus the trap voltage V_t and the resonator-guard voltage V_{rg} . The amplitude drops when the electron's transition frequency f_q is tuned on resonance with the resonator. **b**, Normalized $(A/A_0)^2$ versus the detuned probe frequency $\Delta f_p = f_p - f_r$

and resonator-guard voltage ΔV_{rg} detuned from the resonance condition in the region indicated by the white horizontal arrows in **a** with fixed V_t . **c**, Line cut from **b** along the white dashed line when the qubit frequency f_q is on resonance with the resonator frequency f_r . The two peaks show the vacuum Rabi splitting, giving the coupling strength $g/2\pi = 3.5$ MHz and intrinsic electron linewidth $\gamma/2\pi \approx 1.7$ MHz, fitted by input–output theory with the known resonator linewidth $\kappa/2\pi = 0.4$ MHz.

applied with positive voltage, plugs into the open end of the ‘resonator’. Four ‘guard’ electrodes, called the ‘trap guards’ and ‘res (resonator) guards’ surrounding the trap, applied with voltages in pairs, provide precise tuning to the trapping potential and thus the electron transition frequency about the resonator frequency. The trap and resonator reside inside an approximately 4 mm long etched channel.

Figure 1e details the structure of this hybrid circuit QED device. The double-stripline resonator is coupled with coplanar waveguides with the input and output coupling rates κ_{in} and κ_{out} , respectively, in a transmission measurement configuration. Each d.c. electrode, biased at V_r , V_t , V_{rg} and V_{tg} , respectively, has its own on-chip low-pass LC filter that isolates the electron and resonator from the d.c. electrodes at microwave frequencies to protect the qubit lifetime and resonator quality factor. We fill liquid Ne into the experimental cell at 26 K and cool down to 10 mK. The shift of resonator frequency f_r can be used to infer the Ne thickness. When the channel is fully filled with Ne, f_r shifts from 6.4266 GHz to 6.2795 GHz (Fig. 1f). In practice, we only put in a tiny amount of Ne to coat the device surface, resulting in a frequency shift of only 0.3–0.6 MHz and an estimated Ne thickness of 5–10 nm from numerical simulations. The observed resonator linewidth $\kappa/2\pi = 0.4$ MHz, which is independent of the Ne filling, indicates a quality factor $Q \approx 1.6 \times 10^4$. Electrons are generated through thermionic emission from a pair of tungsten filaments inside the cell under a voltage pulse train (with width of 0.1 ms, height of 4 V and repetition rate of 1 kHz) for a total duration of 1 s (refs. ^{17,18}) (see Methods for more details).

Strong coupling and vacuum Rabi splitting

We use a similar scheme as in our previous work¹⁸ to load single electrons onto the trap from the channel hosting the stripline resonator, while monitoring the microwave transmission signal. Once an electron is trapped, we fix the resonator voltage V_r at 1 V and the trap-guard voltage V_{tg} at 0 V. A positive V_r is necessary to keep any remnant electrons inside the long channel far from resonance. The trap voltage V_t and resonator-guard voltage V_{rg} are enough to tune the qubit frequency f_q into resonance with the resonator frequency $f_r \approx 6.426$ GHz. Figure 2a gives a colour plot of the normalized transmission amplitude $(A/A_0)^2$ probed at the resonator frequency f_r versus the tuning voltages V_t and V_{rg} for a trapped electron. When f_q is tuned across f_r , we observe a sharp drop in the microwave transmission amplitude probed at f_r (ref. ¹⁴). The average photon occupancy in the resonator is controlled at the single-photon level, $\bar{n} \approx 1$, with about −135 dBm input power to the resonator (see Methods for details).

By measuring the transmission spectrum as a function of probe frequency f_p near the resonator frequency f_r , we observe a clear avoided crossing—vacuum Rabi splitting—when V_t is fixed and V_{rg} tunes the qubit frequency across the resonator frequency (Fig. 2b). Figure 2c shows the line cut of Fig. 2b in the on-resonance case $f_q = f_r$. A fit over the two peaks by input–output theory⁶¹ yields a coupling strength of $g/2\pi = 3.5$ MHz, which is nearly twice the electron dephasing rate of $\gamma/2\pi \approx 1.7$ MHz, with a known resonator decay rate of $\kappa/2\pi \approx 0.4$ MHz (see Methods for details). The system has clearly entered the strong coupling regime¹⁴, $g > \gamma, \kappa$, which subsequently enables coherent microwave control and dispersive readout of single-electron qubits in this system.

Spectroscopy and time-domain characterization

Figure 3a shows a two-tone qubit spectroscopy measurement of another trapped electron, which has a stronger coupling strength and a wider electron linewidth than the previous one. The qubit frequency f_q is tuned by the resonator-guard voltage V_{rg} . At each given V_{rg} , we monitor the transmission phase ϕ at the bare resonator frequency f_r , while a pump-tone frequency f_s is slowly swept over a range of approximately 1 GHz across the qubit frequency f_q . When f_s is resonant with f_q , it partially excites the qubit, inducing a dip ($f_q < f_s$) or a peak ($f_q > f_s$) in the ϕ versus f_s plot (Fig. 3a, inset). By scanning both f_s and V_{rg} , we obtain the intrinsic qubit spectrum as a function of V_{rg} . A Lorentzian fit of this qubit spectrum yields a linewidth of $\gamma/2\pi = 2.8$ MHz. The pump-tone power is kept low enough here to avoid power broadening of the qubit over its natural linewidth. The overall spectrum resembles that of a double-quantum-dot (DQD) qubit spectrum at a semiconductor interface²⁶. See Methods for further discussions.

By increasing the pump-tone power, we investigate the anharmonicity under a varied detuning of $\Delta/2\pi = f_q - f_r$ between −100 MHz and +100 MHz. At a detuning of −100 MHz, the measured anharmonicity between the two lowest transition frequencies is $\alpha/2\pi = f_{|1\rangle \rightarrow |2\rangle} - f_{|0\rangle \rightarrow |1\rangle} \approx 40$ MHz, where $|0\rangle$, $|1\rangle$ and $|2\rangle$ are the ground, first-excited and second-excited states, respectively (Methods). This α is positive and consistent with the value expected from the trap design¹⁸. Even though this α value currently limits single qubit gate durations to $t_\pi \gg \pi/\alpha \approx 12$ ns, it can be easily enhanced in future trap designs.

The measured coupling strength for this electron is $g/2\pi = 4.5$ MHz (Methods). At a large detuning of $\Delta/2\pi = -100$ MHz, we have $|\Delta| \gg g$. The dispersive coupling between the qubit and resonator provides a qubit-state-dependent frequency shift of χ . By measuring the transmission phase ϕ of the photons at f_r , we can read out the qubit state^{49,62}.

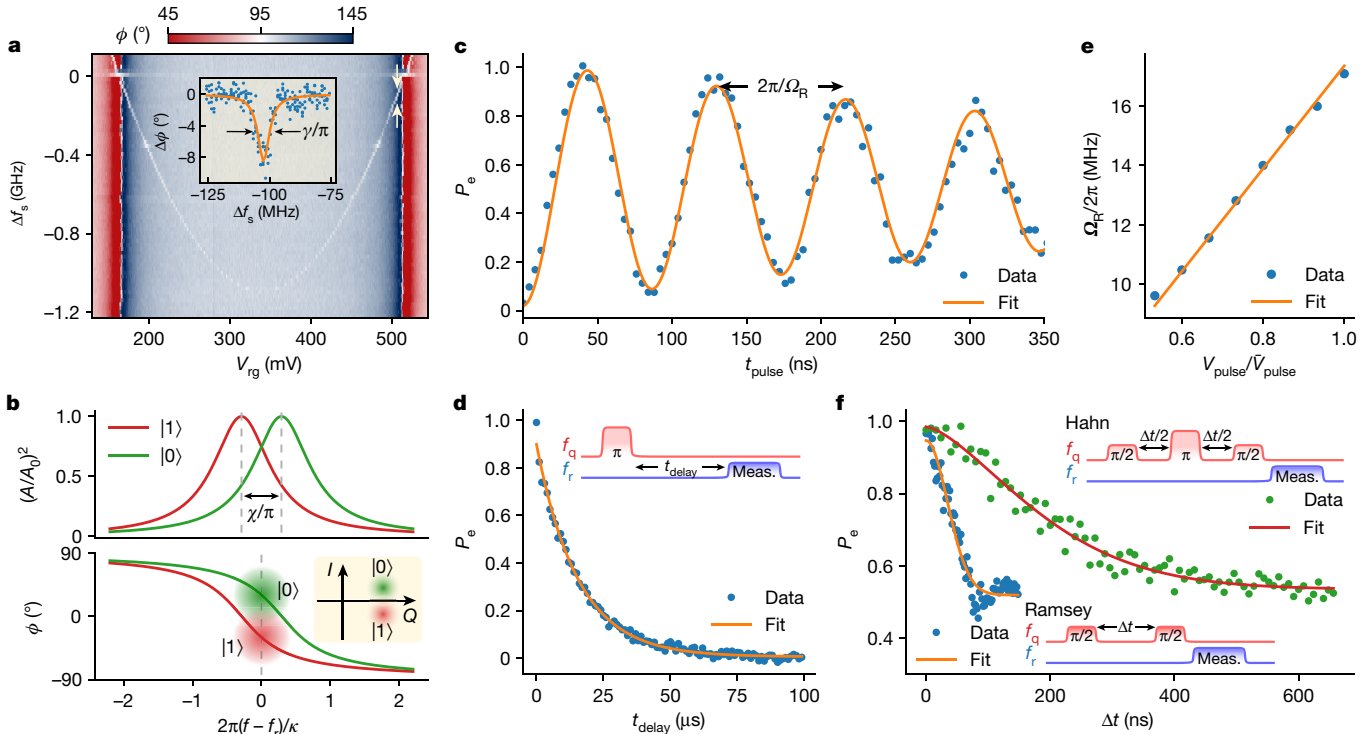


Fig. 3 | Spectroscopy and time-domain characterization of a single-electron qubit on solid neon. **a**, Two-tone qubit spectroscopy measurement on the transmission phase ϕ at the resonator frequency f_r versus the detuned pump frequency $\Delta f_s = f_s - f_r$ and the resonator-gate voltage V_{rg} . The qubit linewidth γ can be obtained by fitting the phase dip profile (inset). **b**, Illustration of the dispersive readout of single-electron qubit state by transmission measurement. Ground and excited electron states cause the actual resonator frequency to be blueshifted and redshifted and the measured

transmission phase ϕ at the bare resonator frequency f_r to show on average $\pm 30^\circ$ shift. **c**, Rabi oscillations of the excited state population P_e , measured at fixed pulse amplitude and varied pulse length t_{pulse} . **d**, Qubit relaxation measurement (meas.) with the fitted relaxation time $T_1 = 15 \mu\text{s}$. **e**, Measured linear dependence of Rabi frequency Ω_R on the amplitude of gate pulses. **f**, Ramsey fringe and Hahn echo measurements with the fitted original coherence time $T_2^* = 50 \text{ ns}$ and extended coherence time $T_{2E} = 220 \text{ ns}$. Qubit detuning for **b–f** is kept at $\Delta/2\pi = f_q - f_r = -100 \text{ MHz}$.

Figure 3b illustrates the scheme of dispersive readout in accordance with our experiment, as is common in circuit QED platforms⁵⁰. The measured ϕ shift at f_r is about $\pm 30^\circ$ after statistical averaging, corresponding to $\chi/2\pi \approx 0.12 \text{ MHz}$. Ideally, the qubit would operate at the minimum of the spectrum of Fig. 3a, that is, the ‘sweet spot’ at which the charge noise has the lowest effect. However, for this particular electron at the ‘sweet spot’, the large detuning of more than 1 GHz precludes state readout with reasonable signal-to-noise ratio.

We now use real-time coherent control to measure the coherence properties of the qubit at a detuning of $\Delta/2\pi = -100 \text{ MHz}$. Figure 3c displays Rabi oscillations in the excited-state population P_e (ref. ⁶³). Starting with the qubit in its ground state, we apply a pulse with variable duration and fixed amplitude at the qubit frequency f_q , immediately followed by a readout pulse applied at the resonator frequency f_r . Figure 3d displays the measurement of the relaxation time T_1 , where we use a π pulse (with duration inferred from Fig. 3c) and vary the delay t_{delay} between the end of each π pulse and the onset of the readout pulse. The population curve fitted by $\exp(-t/T_1)$ yields $T_1 = 15 \mu\text{s}$, which is long compared with most semiconductor charge qubits²¹. We also verify the linear dependence of the Rabi frequency Ω_R on the pulse amplitude V_{pulse} normalized by the maximally used amplitude \bar{V}_{pulse} (Fig. 3e).

Figure 3f shows the measurements of the original (Ramsey fringe) coherence time T_2^* and extended (Hahn echo) coherence time T_{2E} (ref. ⁶³) (see Methods for details). The Ramsey measurement consists of two $\pi/2$ pulses separated by a varied delay time of Δt . The population curve is found to be best fitted by a Gaussian decay function of $\exp[-(t/T_2^*)^2]$ with $T_2^* = 50 \text{ ns}$, which is consistent with the linewidth from the two-tone spectroscopy measurement. The Ramsey measurement is known to be sensitive to low-frequency electromagnetic fluctuations in the

circuit. The Hahn echo measurement inserts an additional π pulse in the middle point between two $\pi/2$ pulses. It mitigates low-frequency noise and transfers the decay function from a Gaussian to an exponential. Our Hahn echo population curve is best fitted with $\exp[-(t/T_{2E})^{1.5}]$ (refs. ^{64,65}), which yields an extended (echo) coherence time of $T_{2E} = 220 \text{ ns}$. These results indicate that the qubit coherence may be primarily limited by low-frequency charge noise.

Discussion and outlook

The long values of T_1 indicate that solid Ne can indeed serve as an ultraclean substrate for single-electron qubits. We expect future trap geometries and better filtering for d.c. electrodes to give even longer values of T_1 . The still short $T_2 \ll T_1$ at this initial stage of development may originate from two sources of residual noise. First, remnant electrons along the resonator in the long channel are not entirely fixed; the remaining motion can cause background charge noise in the trapped electron–photon interacting system. Second, Ne atoms on an imperfect (presumably rough and porous) surface can be highly movable and induce a time-varying trapping potential on the electron. Improvement of the device design and Ne growth process⁵¹, and operation at the charge noise ‘sweet spot’ are expected to mitigate these decoherence issues. It has been theoretically calculated that the in-plane motional coherence of an electron on a solid Ne surface can be several milliseconds⁵⁵. Ultimately, using the spin states by engineered spin–orbital coupling^{16,27} can yield an ultralong qubit coherence in excess of 1 s (refs. ^{12,16,19,51}).

The strong interaction between the electron motional states and the microwave photons will enable two or more electrons to entangle

with each other through exchanging (virtual) photons in the resonator. To scale the system up, we can adopt the quantum charge-coupled device technique, originally developed for a trapped ion system^{13,33,36}, to shuffle electrons into and out of different functional zones on a chip to achieve multi-electron gating, entanglement and readout. This will significantly expand the scalability.

The eNe qubit platform incorporates compelling advantages from several leading qubit platforms. First, analogous to electromagnetically trapped ions, the electron qubits here are identically generated by a simple source and can have long spin coherence times. Second, as with semiconductor quantum dots, electronic gate control can be applied at high speed. Finally, strong coupling with the circuit QED architecture enables dispersive readout, transduction to microwave photons and two-qubit gates through microwave resonator mediated interactions. Given these merits, we anticipate that the eNe qubit platform will rapidly develop into a superior quantum computing hardware. Furthermore, the eNe qubit can be linked with other quantum information systems such as Josephson junction qubits and colour centres via the microwave interface. With this, we expect the eNe qubit platform to collectively advance quantum sensing, transduction, networks and other important areas in quantum science and fundamental physics.

Online content

Any methods, additional references, Nature Research reporting summaries, source data, extended data, supplementary information, acknowledgements, peer review information; details of author contributions and competing interests; and statements of data and code availability are available at <https://doi.org/10.1038/s41586-022-04539-x>.

1. Ladd, T. D. et al. Quantum computers. *Nature* **464**, 45–53 (2010).
2. Popkin, G. Quest for qubits. *Science* **354**, 1090–1093 (2016).
3. de Leon, N. P. et al. Materials challenges and opportunities for quantum computing hardware. *Science* **372**, 253 (2021).
4. Hanson, R., Kouwenhoven, L. P., Petta, J. R., Tarucha, S. & Vandersypen, L. M. Spins in few-electron quantum dots. *Rev. Mod. Phys.* **79**, 1217–1265 (2007).
5. Zwanenburg, F. A. et al. Silicon quantum electronics. *Rev. Mod. Phys.* **85**, 961–1019 (2013).
6. Cole, M. W. & Cohen, M. H. Image-potential-induced surface bands in insulators. *Phys. Rev. Lett.* **23**, 1238 (1969).
7. Cole, M. W. Electronic surface states of a dielectric film on a metal substrate. *Phys. Rev. B* **3**, 4418 (1971).
8. Leiderer, P. Electrons at the surface of quantum systems. *J. Low Temp. Phys.* **87**, 247–278 (1992).
9. Platzman, P. & Dykman, M. I. Quantum computing with electrons on liquid helium. *Science* **284**, 1967–1969 (1999).
10. Smolyaninov, I. I. Electrons on solid hydrogen and solid neon surfaces. *Int. J. Mod. Phys. B* **15**, 2075–2106 (2001).
11. Dykman, M. I., Platzman, P. M. & Seddighrad, P. Qubits with electrons on liquid helium. *Phys. Rev. B* **67**, 155402 (2003).
12. Lyon, S. A. Spin-based quantum computing using electrons on liquid helium. *Phys. Rev. A* **74**, 052338 (2006).
13. Bradbury, F. R. et al. Efficient clocked electron transfer on superuid helium. *Phys. Rev. Lett.* **107**, 266803 (2011).
14. Wallraff, A. et al. Strong coupling of a single photon to a superconducting qubit using circuit quantum electrodynamics. *Nature* **431**, 162–167 (2004).
15. Blais, A., Girrsmo, A. L. & Wallraff, A. Circuit quantum electrodynamics. *Rev. Mod. Phys.* **93**, 025005 (2021).
16. Schuster, D. I., Fragner, A., Dykman, M. I., Lyon, S. A. & Schoelkopf, R. J. Proposal for manipulating and detecting spin and orbital states of trapped electrons on helium using cavity quantum electrodynamics. *Phys. Rev. Lett.* **105**, 040503 (2010).
17. Yang, G. et al. Coupling an ensemble of electrons on superfluid helium to a superconducting circuit. *Phys. Rev. X* **6**, 011031 (2016).
18. Koolstra, G., Yang, G. & Schuster, D. I. Coupling a single electron on superfluid helium to a superconducting resonator. *Nat. Commun.* **10**, 5323 (2019).
19. Jin, D. Quantum electronics and optics at the interface of solid neon and superfluid helium. *Quantum Sci. Technol.* **5**, 035003 (2020).
20. Clerk, A. A., Lehnert, K. W., Bertet, P., Petta, J. R. & Nakamura, Y. Hybrid quantum systems with circuit quantum electrodynamics. *Nat. Phys.* **16**, 257–267 (2020).
21. Chatterjee, A. et al. Semiconductor qubits in practice. *Nat. Rev. Phys.* **3**, 157–177 (2021).
22. Nakamura, Y., Pashkin, Y. A. & Tsai, J. S. Coherent control of macroscopic quantum states in a single-cooper-pair box. *Nature* **398**, 786–788 (1999).
23. Schoelkopf, R. J. & Girvin, S. M. Wiring up quantum systems. *Nature* **451**, 664–669 (2008).
24. Clarke, J. & Wilhelm, F. K. Superconducting quantum bits. *Nature* **453**, 1031–1042 (2008).
25. Arute, F. et al. Quantum supremacy using a programmable superconducting processor. *Nature* **574**, 505–510 (2019).
26. Kawakami, E. et al. Electrical control of a long-lived spin qubit in a Si/SiGe quantum dot. *Nat. Nanotechnol.* **9**, 666–670 (2014).
27. Mi, X. et al. A coherent spin-photon interface in silicon. *Nature* **555**, 599–603 (2018).
28. Samkharadze, N. et al. Strong spin-photon coupling in silicon. *Science* **359**, 1123–1127 (2018).
29. Landig, A. J. et al. Coherent spin-photon coupling using a resonant exchange qubit. *Nature* **560**, 179–184 (2018).
30. Petit, L. et al. Universal quantum logic in hot silicon qubits. *Nature* **580**, 355–359 (2020).
31. Burkard, G., Gullans, M. J., Mi, X. & Petta, J. R. Superconductor-semiconductor hybrid-circuit quantum electrodynamics. *Nat. Rev. Phys.* **2**, 129–140 (2020).
32. Monroe, C., Meekhof, D. M., King, B. E., Itano, W. M. & Wineland, D. J. Demonstration of a fundamental quantum logic gate. *Phys. Rev. Lett.* **75**, 4714 (1995).
33. Kielinski, D., Monroe, C. & Wineland, D. J. Architecture for a large-scale ion-trap quantum computer. *Nature* **417**, 709–711 (2002).
34. Leibfried, D., Blatt, R., Monroe, C. & Wineland, D. Quantum dynamics of single trapped ions. *Rev. Mod. Phys.* **75**, 281 (2003).
35. Bruzewicz, C. D., Chiaverini, J., McConnell, R. & Sage, J. M. Trapped-ion quantum computing: Progress and challenges. *Appl. Phys. Rev.* **6**, 021314 (2019).
36. Pino, J. M. et al. Demonstration of the trapped-ion quantum CCD computer architecture. *Nature* **592**, 209–213 (2021).
37. Brennen, G. K., Caves, C. M., Jessen, P. S. & Deutsch, I. H. Quantum logic gates in optical lattices. *Phys. Rev. Lett.* **82**, 1060 (1999).
38. Jaksch, D. et al. Fast quantum gates for neutral atoms. *Phys. Rev. Lett.* **85**, 2208 (2000).
39. Saffman, M., Walker, T. G. & Mølmer, K. Quantum information with Rydberg atoms. *Rev. Mod. Phys.* **82**, 2313–2363 (2010).
40. Wang, Y., Kumar, A., Wu, T.-Y. & Weiss, D. S. Single-qubit gates based on targeted phase shifts in a 3D neutral atom array. *Science* **352**, 1562–1565 (2016).
41. Pla, J. J. et al. A single-atom electron spin qubit in silicon. *Nature* **489**, 541–545 (2012).
42. Pla, J. J. et al. High-fidelity readout and control of a nuclear spin qubit in silicon. *Nature* **496**, 334–338 (2013).
43. Chen, S., Raha, M., Phenice, C. M., Ourari, S. & Thompson, J. D. Parallel single-shot measurement and coherent control of solid-state spins below the diffraction limit. *Science* **370**, 592–595 (2020).
44. Wolfowicz, G. et al. Quantum guidelines for solid-state spin defects. *Nat. Rev. Mater.* **6**, 906–925 (2021).
45. Vincent, R., Klyatskaya, S., Ruben, M., Wernsdorfer, W. & Balestro, F. Electronic readout of a single nuclear spin using a molecular spin transistor. *Nature* **488**, 357–360 (2012).
46. Thiele, S. et al. Electrically driven nuclear spin resonance in single-molecule magnets. *Science* **344**, 1135–1138 (2014).
47. Atzori, M. & Sessoli, R. The Second Quantum Revolution: Role and Challenges of Molecular Chemistry. *J. Am. Chem. Soc.* **141**, 11339–11352 (2019).
48. Coronado, E. Molecular magnetism: from chemical design to spin control in molecules, materials and devices. *Nat. Rev. Mater.* **5**, 87–104 (2020).
49. Schuster, D. I. et al. ac Stark shift and dephasing of a superconducting qubit strongly coupled to a cavity field. *Phys. Rev. Lett.* **94**, 123602 (2005).
50. Wallraff, A. et al. Approaching unit visibility for control of a superconducting qubit with dispersive readout. *Phys. Rev. Lett.* **95**, 060501 (2005).
51. Sheludakov, S. et al. Electrons trapped in solid neon-hydrogen mixtures below 1 K. *J. Low Temp. Phys.* **195**, 365–377 (2019).
52. Jacobsen, R. T., Penncello, S. G. & Lemmon, E. W. In *Thermodynamic Properties of Cryogenic Fluids* (eds Weisled II, J. G. & Jeong S.) 31–287 (Springer, 1997).
53. Pollack, G. L. The solid state of rare gases. *Rev. Mod. Phys.* **36**, 748 (1964).
54. Batchelder, D. N., Losee, D. L. & Simmons, R. O. Measurements of lattice constant, thermal expansion, and isothermal compressibility of neon single crystals. *Phys. Rev.* **162**, 767 (1967).
55. Zavyalov, V., Smolyaninov, I., Zotova, E., Borodin, A. & Bogomolov, S. Electron states above the surfaces of solid cryodielectrics for quantum-computing'. *J. Low Temp. Phys.* **138**, 415–420 (2005).
56. Leiderer, P., Kono, K. & Rees, D. In *Proc. 11th International Conference on Cryocrystals and Quantum Crystals* (ed. Vasiliev, S.) 67–67 (University of Turku, 2016).
57. Kajita, K. A new two-dimensional electron system on the surface of solid neon. *Surf. Sci.* **142**, 86–95 (1984).
58. Nilsson, A., Pettersson, L. G. & Norskov, J. *Chemical Bonding at Surfaces and Interfaces* (Elsevier, 2011).
59. Ibach, H. *Physics of Surfaces and Interfaces Vol. 2006* (Springer, 2006).
60. Pozar, D. M. *Microwave Engineering* (Wiley, 2011).
61. Walls, D. F. & Milburn, G. J. *Quantum Optics* (Springer Science & Business Media, 2007).
62. Schuster, D. I. *Circuit Quantum Electrodynamics* PhD thesis, Yale Univ. (2007).
63. Krantz, P. et al. A quantum engineer's guide to superconducting qubits. *Appl. Phys. Rev.* **6**, 021318 (2019).
64. Ithier, G. et al. Decoherence in a superconducting quantum bit circuit. *Phys. Rev. B* **72**, 134519 (2005).
65. Chen, Z. *Metrology of Quantum Control and Measurement in Superconducting Qubits* PhD thesis, Univ. of California Santa Barbara (2018).

Publisher's note Springer Nature remains neutral with regard to jurisdictional claims in published maps and institutional affiliations.

© UChicago Argonne, LLC, Operator of Argonne National Laboratory, under exclusive licence to Springer Nature Limited 2022

Methods

Cryostat setup

Our experiment is performed in a BlueFors LD400 dilution refrigerator system with a base temperature of about 7 mK. Extended Data Figure 1 shows our cryostat and measurement setup for single-electron qubits on solid Ne in a circuit QED architecture. In this section, we focus on the cryostat setup inside the fridge. The measurement setup outside the fridge is explained in later sections when it is referred to.

All the input radiofrequency (RF) coaxes are made of silver-plated beryllium copper (SBeCu) from the room temperature (RT) plate (that is, the 300 K plate) all the way to the mixing chamber (MXC) plate (that is, the 10 mK plate). The output coaxes are made of SBeCu from the RT plate to the 3 K plate but are made of superconducting niobium titanium (NbTi) from the 3 K plate to the MXC plate. Attenuators are installed along every RF line at every temperature stage to thermalize the cables and reduce the noise that comes from the instrument at RT. For the input lines, there is an attenuation of 20 dB at 3 K, 10 dB at 1 K, 10 dB at 100 mK and 20 dB at 10 mK. For the output lines, only an attenuation of 0 dB is used at every temperature stage for thermal anchoring. A 4–12 GHz cryogenic dual-junction isolator (Low-Noise Factory LNF-ISIC4_12A) with an isolation of 30 dB is installed at the output of the sample cell to block the thermal noise from higher temperatures. The isolator is followed by a 4–12 GHz cryogenic circulator (LNF-CIC4_12A) with 50 Ω termination giving another isolation of 20 dB. A 4–8 GHz high-electron-mobility transistor amplifier (LNF-LNC4_8C) with a gain of 39 dB and a noise temperature of 2 K is installed on the 3 K plate. Immediately outside the fridge, a 4–23 GHz RT low-noise amplifier (LNF-LNR4_23A) with a gain of 27 dB and a noise temperature of 65 K (measured at 6 GHz) serves as the first-stage RT amplifier.

There are two types of d.c. ($\lesssim 1$ kHz) lines installed in our fridge: first, thermocoaxes with the inner core and outer shield made of stainless steel and the dielectric filling made of magnesium oxide (MgO) powder; second, twisted-pair d.c. wires consisting of phosphor bronze (PhBr) between the RT and 3 K plates and superconducting NbTi wires between the 3 K and MXC plates.

The d.c. voltages that control the electron trap and qubit detuning are delivered through thermocoaxes. They each provide an attenuation of more than 35 dB above 100 MHz. At the MXC plate, behind each thermocoax there is a two-stage RC low-pass filter with a cutoff frequency of around 400 Hz cascaded with a LC low-pass filter (Mini-Circuits RLP-30+) with a cutoff frequency of around 30 MHz. The voltage and current to generate electrons from the tungsten filaments are delivered through the twisted-pair wires.

A stainless steel fill line, consisting of two sections, is built in the fridge to fill Ne into a sample cell. The first section has a length of 2 m and an inner diameter of 0.6 mm, running from the RT plate down to beneath the 3 K plate, being heat sunk at the 50 K plate and the 3 K plate. The second section has another length of 2 m, with inner diameter of 0.24 mm, running from the end of the first section down to beneath the MXC plate, being heat sunk on the still plate (that is, the 1 K plate), the cold plate (that is, the 100 mK plate) and the MXC plate. Then the fill line is converted into a brass flange, which interfaces through an indium seal with another brass flange from the sample cell.

The sample cell consists of a copper lid and a copper pedestal, as shown in Extended Data Fig. 2. The lid contains 14 hermetic SMP feedthroughs (Corning 0119-783-1) for the d.c. and RF signals, 2 SMP feedthroughs for the electron source and a stainless steel tube (1/16" outer diameter and 0.021" inner diameter) for the Ne filling. A custom-designed printed circuit board along with a 2 × 7 mm sample chip is mounted on the pedestal inside the cell. The SMP connectors on the printed circuit board are connected to the hermetic SMP connectors on the lid through SMP bullets (Rosenberger 19K106-K00L5). The lid and pedestal are sealed together by indium wires.

Two tungsten filaments are taken from standard 1.5 V miniature bulbs and mounted in parallel above the sample chip inside the sample cell (Extended Data Fig. 2). The wire and coil diameter of the filament are 4 μm and 25 μm, respectively. There are about 30 coils for each filament. The resistance of each filament at RT is 15 Ω.

Preparation experiments

Extended Data Figure 3 gives the phase diagram of neon. We use research-grade (99.999% purity) Ne gas from Airgas. We fill Ne into the cell by first warming up the temperature of the 3 K plate to 25.6–26.4 K and of the cell at the MXC plate to 25.5 K. The back-end pressure at the Ne tank is 10 psi above atmospheric pressure. Neon gas flows through a liquid nitrogen (LN₂) cold trap to remove any potential impurity that may clog the fill line. Then it reaches a volume control unit consisting of two solenoid valves (IMI Norgren U142010 24VDC), a pressure transducer (Swagelok PTI-S-AG60-22AQ) and a 10 ml cylinder (Swagelok SS-4CS-TW-10). Neon turns into liquid at the 3 K plate and drips into the cell along the second section of fill line. We estimate the amount of filled Ne by counting the number of puffs by repeatedly opening and closing the valves. Each puff corresponds to 10 ml of Ne gas at room temperature.

The effective permittivity of the stripline resonator changes with the amount of Ne filled inside the channel. After filling, we gradually reduce the heating power to let the cell slowly cool across the triple point and then continue cooling down to 10 mK. By measuring the resonance frequency shift and comparing it with our numerical simulation, we can estimate the Ne thickness. In a typical experiment, we only send in about 40 puffs, which coat about 5–10 nm of solid Ne on the device surface and induce a frequency shift of only 0.3–0.6 MHz.

It is worth mentioning that even though a solid Ne cryogenic substrate can exist at approximately 20 K, operation of a circuit QED architecture still requires much lower temperatures to attain superconductivity and high-*Q* resonances. Although we imagine that the device might operate at temperatures of a few Kelvin, these temperatures would correspond to a thermal environment for frequencies of approximately 6 GHz of the qubit and resonator, making operation more challenging.

A vector network analyzer (VNA) (Keysight E5071C) is used to carry out the microwave transmission measurement through the superconducting stripline resonator. Ports 1 and 2 of the VNA are connected to the input and output RF lines, respectively, of the device inside the fridge. This constitutes a standard forward-transmission-coefficient S_{21} measurement. We took a separate reference measurement without the device and found the total attenuation from port 1 of the VNA to the sample input to be about 70 dB, including the RT part of the cable loss.

The experimental transmission amplitude $(A/A_0)^2$ of the resonator is fitted with the Lorentzian function

$$(A/A_0)^2 = \frac{(\kappa/2\pi)^2}{4(f-f_r)^2 + (\kappa/2\pi)^2}, \quad (1)$$

where f_r is the resonator frequency and $\kappa/2\pi$ is the linewidth. The transmission phase ϕ is

$$\phi = \arctan \frac{4\pi(f-f_r)}{\kappa}. \quad (2)$$

The measured resonator frequency f , without Ne is 6.4266 GHz. The measured resonator linewidth κ is $2\pi \times 0.4$ MHz, giving a quality factor $Q \approx 1.6 \times 10^4$. Fully filling the channel with Ne shifts the resonance to 6.2795 GHz, whereas a coating of the device surface of 5–10 nm only slightly shifts the resonance towards 6.426 GHz. With and without Ne, no significant change in κ or Q is observed.

The average photon occupancy \bar{n} in the resonator is critical to our measurements. According to input–output theory⁶¹, it can be estimated by

Article

$$\bar{n} = \frac{\kappa_{\text{in}}}{hf_r(\kappa_{\text{in}} + \kappa_{\text{out}} + \kappa_i)^2} P_{\text{in}}, \quad (3)$$

where P_{in} is the input power, κ_{in} and κ_{out} are the input and output coupling rates, respectively, and κ_i is the intrinsic loss. For a typical over-coupled symmetric two-port superconducting stripline resonator, $\kappa_{\text{in}} \approx \kappa_{\text{out}} \gg \kappa_i$. Thus, the overall linewidth $\kappa \approx \kappa_{\text{in}} + \kappa_{\text{out}} \approx 2\kappa_{\text{in}}$, and the average photon number can be simplified to

$$\bar{n} = \frac{P_{\text{in}}}{2hf_r\kappa}. \quad (4)$$

In our case, with a measured resonator frequency of $f_r \approx 6.426$ GHz, a linewidth of $\kappa/2\pi = 0.4$ MHz and a desired occupancy of $\bar{n} \approx 1$, we can find the required input power of $P_{\text{in}} \approx -135$ dBm.

Electrons are generated by applying voltage and current to the two filaments in parallel using a low-frequency function generator (Agilent 33220A). The driving pattern is a pulse train of width 0.1 ms, height 4 V and repetition rate 1 kHz for a duration time of 1 s.

A digital-to-analogue converter (NI-6363) provides all the d.c. voltages, including the resonator voltage V_r , trap voltage V_t , resonator-guard voltage V_{rg} and trap-guard voltage V_{tg} , through thermocoaxes. When generating electrons through tungsten filaments, we fix $(V_r, V_t, V_{rg}, V_{tg}) = (1, 0, 0, 0)$ V and monitor the evolution of the transmission spectrum with the VNA, as shown in Extended Data Fig. 4. The positive V_r helps to attract electrons into the channel. After the initial electron injection, the spectrum undergoes a sudden change with a large resonance frequency shift. After a few seconds, the resonance peak is restored back to close to the starting frequency. However, too many electrons may have been deposited onto the trap and resonator in the channel. To remove most of the redundant electrons, we reverse V_r to a large negative voltage to repel electrons away. This eventually brings the resonance frequency back very close to the bare resonator frequency with very few electrons remaining on the trap and resonator. At this point, we switch V_r back to +1 V to keep unwanted electrons in the channel far from resonance with the resonator, and therefore minimize the charge noise from the channel.

We use the procedure given in our previous work to load individual electrons from the resonator (reservoir) onto the trap¹⁸. This procedure involves a complex d.c. voltage tuning sequence. During this procedure, we watch the change in microwave transmission from the VNA at the bare resonator frequency f_r . As the number and position of the electrons in the channel are not completely deterministic, we cannot yet guarantee that every loading process captures a single electron. Sometimes, we have to repeat the electron generation process. However, our overall successful rate is very high.

After each loading procedure, we fix the resonator voltage $V_r = 1$ V and trap-guard voltage $V_{tg} = 0$ V and fine scan the resonator-guard voltage V_{rg} and trap voltage V_t in a wide range spanning several hundreds of millivolts. If a single electron is indeed present, we can observe one or two sharp absorption lines. Those lines correspond to the case when the qubit frequency f_q matches the resonator frequency f_r so as to induce transmission absorption. Extended Data Figure 5 displays the observed absorption lines corresponding to the electron qubit presented in Fig. 3.

Frequency-domain measurements

In the vacuum Rabi splitting measurement, we keep the VNA setup unchanged from the transmission measurement above. The probe frequency f_p of the VNA is sweeping around the bare resonator frequency in a narrow range of $f_r \pm 10$ MHz, while the resonator-guard voltage V_{rg} is tuned by ± 1 mV from the on-resonance value. All other voltages are fixed. In the plot of normalized transmission amplitude $(A/A_0)^2$ versus f_p and V_{rg} , the avoided crossing is sharpest when the qubit and resonator are coupled on resonance. The splitting between the

two transmission peaks in this on-resonance condition yields the coupling constant $2g/2\pi$. In this measurement, to avoid power broadening, the probe power is kept low according to equation (4) so that the average photon occupancy \bar{n} inside the cavity is about 1.

The vacuum Rabi splittings corresponding to the electron qubit presented in Fig. 3 is shown in Extended Data Fig. 6. According to input-output theory⁶¹, the transmission spectrum of the coupled system reads

$$S_{21} = \frac{\kappa/2}{i2\pi(f_r - f_p) + \kappa/2 + ig^2/(2\pi f_q - 2\pi f_p - iy)}, \quad (5)$$

under the assumption that the resonator intrinsic decay rate κ_i is much less than the input and output coupling rates $\kappa_{\text{in}} = \kappa_{\text{out}} = \kappa/2$. With this formula, the fitted coupling strength is $g = 2\pi \times 4.5$ MHz and the electron linewidth is $y = 2\pi \times 3.4$ MHz. The latter is slightly larger than that obtained through two-tone qubit spectroscopy.

In the two-tone qubit spectroscopy measurement, the VNA provides the first tone, that is, the probe tone, and a signal generator (Anritsu MG3692C) provides the second tone, that is, the pump tone. The qubit spectrum is tuned by the resonator-guard voltage V_{rg} . The VNA setup is the same as before. Ports 1 and 2 of the VNA are connected to the input and output lines of the device, but the probe frequency is fixed only at the bare resonator frequency $f_r = 6.426$ GHz and is not swept. The signal generator generates a continuous wave at the pump frequency f_s that is swept over a broad range from $f_r - 1.2$ GHz to $f_r + 0.2$ GHz. This pump tone is combined with the signal from port 1 of VNA and sent into the input line of the device inside the fridge. The combination is made through a directional coupler. The pump tone goes into the coupled port of the directional coupler with a signal reduction of -10 dB. For each given V_{rg} , f_s is swept to produce the qubit spectrum for that particular V_{rg} . Then V_{rg} is scanned over a range of several hundreds of millivolts. The transmission phase at f_s is recorded as a function of both V_{rg} and f_s , and generates a complete qubit spectrum.

When the pump frequency f_s is far detuned from the resonator frequency f_r , the resonator suppresses the pump amplitude and increases the required power. In our experiments, we apply a pump power of -10 dBm from the signal generator. Taking account of the 70 dB attenuation on the input line and the 10 dB coupling of the directional coupler, the input pump power at the sample is -90 dBm. The measured qubit linewidth is dependent on the pump power, known as power broadening. In practice, we vary the power to attain the narrowest linewidth while maintaining a reasonable signal-to-noise ratio.

To see higher order transitions and gain some insight into the anharmonicity of this qubit, we pump the system even harder. We are able to see many other transitions in the detuning range of ± 100 MHz, which is the main range of interest. Extended Data Figure 7 shows two-tone spectroscopy with high-power qubit pumping. At a detuning of -100 MHz, the anharmonicity between the two lowest transition frequencies is $\alpha/2\pi = f_{|1\rangle \rightarrow |2\rangle} - f_{|0\rangle \rightarrow |1\rangle} \approx 40$ MHz, where $|0\rangle$, $|1\rangle$ and $|2\rangle$ are the ground, first-excited and second-excited states, respectively. This number can provide an estimate of the frequency shift in dispersive readout.

Time-domain measurements

In our time-domain measurements, the qubit frequency is tuned to $f_q = 6.326$ GHz by the d.c. electrodes. Compared with the bare resonator frequency at $f_r = 6.426$ GHz, the qubit-to-resonator detuning is $\Delta/2\pi = f_q - f_r = -100$ MHz.

The following procedure is used to generate qubit gate pulses. The signal generator (Anritsu MG3692C) generates a continuous sine wave at 6.206 GHz, which is 120 MHz below f_q . It is sent into the local oscillator (LO) port of an IQ-mixer (MarkiMMIQ 0520H). An arbitrary waveform generator (Tektronics AWG5204) generates, at its channels 1 and 2, two rectangle-enveloped sine-wave pulse sequences, with the same amplitude, pulse length and 120 MHz central frequency, but different phases offset by $\pi/2$ from each other. They are respectively sent into

the two intermediate frequency (IF) ports, that is, the I and Q ports of the IQ-mixer. The output from the RF port of the IQ-mixer contains only the upper sideband pulse sequence with a carrier frequency at the qubit frequency $f_q = 6.326$ GHz. The lower sideband and the LO sine wave are both suppressed.

The following procedure is used to generate qubit readout pulses. Another signal generator (Lab Brick LMS-183DX) generates a continuous sine wave at the bare resonator frequency $f_r = 6.426$ GHz. It is sent into the LO port of a mixer (MiniCircuit ZMX-8GH). The arbitrary waveform generator generates, from its channel 3, which is synchronized and delayed from channels 1 and 2, a rectangle-enveloped d.c. pulse sequence with appropriate amplitude and typically 2 μ s pulse length. It is sent into the IF port of the mixer. The output from the RF port of this mixer is a rectangle-enveloped pulse sequence with a carrier frequency at the resonator frequency $f_r = 6.426$ GHz. Instead of being sent straight into the fridge, the readout pulse sequence is first sent into the input port of a directional coupler and only a -20 dB portion is split off from the coupler port to go into the fridge. The readout pulse from the output port of the directional coupler serves as a reference signal in the dispersive phase measurement setup.

The qubit gate pulse sequence and the readout pulse sequence are combined through a combiner and sent into the input line of the circuit QED device inside the fridge. Although they travel along the same line, they do not overlap in real time. The transmitted readout pulse sequence, containing the phase information from the dispersive coupling with the qubit, is then routed to the RF port of a second mixer (MiniCircuit ZMX-8GH) for heterodyne detection. A third signal generator (Lab Brick LMS-183DX) provides a continuous sine wave at $f_r + 50$ MHz to the LO port of this mixer. The signal from the IF port is further amplified and sent into channel 2 of a digitizer (Alazar ATS9870). The reference readout pulse from the output port of the directional coupler is routed into the RF port of a third mixer (MiniCircuit ZMX-8GH). The same third signal generator provides the same continuous sine wave to the LO port of this mixer through a splitter. The signal from the IF port of this mixer is sent into channel 1 of the digitizer.

All the time-domain measurements, including Rabi oscillations, T_1 relaxation time and T_2 coherence time measurements follow exactly the same scheme as in the superconducting qubit measurements⁶³ and have been detailed in the main Article. For all the time-domain measurements, statistical results are obtained with an average taken of over 5,000 measurements.

Theoretical analysis

Calculation of the electronic states along the z direction follows the standard procedure of numerically solving a one-dimensional Schrödinger equation¹⁹. In the limit of barrier height $U \rightarrow \infty$ and short-range cutoff $b \rightarrow 0$, the problem can be mapped into that of the radial part of a hydrogen atom to yield an analytical solution⁶⁷. However, compared with eHe, an eNe experiences a 30% lower repulsive barrier but a four times stronger attractive potential, and is much more tightly bound to the surface at a mean distance of only 1–2 nm. Therefore, analytical solutions can have large errors. The results presented in Fig. 1a come from our finite-difference numerical calculation at an extremely fine space step of 0.1 Å. However, even with such a fine step, there are still several important points to be kept in mind. First, the calculated eigenenergies are still sensitive to the accurate choice of U and b because of the divergent nature of the $-1/z$ like polarization potential as $z \rightarrow 0$. There is always a competition between the positive part of the potential at $z \lesssim 0^-$ and the negative part at $z \gtrsim 0^+$, which determines how much wavefunction ‘spills’ into the barrier. A tiny difference in ‘spilling’, even one that is not discernible by looking at the wavefunctions, can cause a large difference in energy. Second, solid neon has a face-centred-cubic crystal structure with a lattice constant of $a = 4.464$ Å, which is not only an order of magnitude larger than our

choice of numerical space step but also larger than the standard choice of cutoff $b \approx \frac{1}{2}a = 2.3$ Å (refs. ^{6,7}). It is not yet clear at what length scale the continuous model used here breaks down and how critically the exact atomic arrangement and surface profile influence the qualitative picture. These questions can, in principle, be addressed by advanced computation methods, such as quantum Monte Carlo simulations, and eventually answered only by experiments.

Here we discuss in more detail the electronic states in the xy plane that are directly related to our experiment. The observed single-electron qubit spectrum in Fig. 3a exhibits a quadratic (parabolic or hyperbolic) curve that is symmetric with respect to a ‘sweet spot’ voltage, $V_{ss} = 339$ mV, in the detuning range of the resonator-guard voltage V_{rg} . This feature qualitatively resembles that of a semiconductor DQD spectrum²⁶. The obtained Extended Data Figs. 5 and 6 for electron–photon coupling and vacuum Rabi splitting also look very similar to those of a DQD qubit²⁶. Although our electron trapping potential was not intended to be a double quantum well, it is actually not a surprise to observe a DQD spectrum, as discussed in more detail below.

Our device was designed to be symmetric with respect to the $y = 0$ plane. In the ideal situation, if an electron is trapped at the centre of the trap and solid neon is grown perfectly flat there, the in-plane trapping potential, after a Taylor expansion in y , should contain only even-order terms, $V(y) \approx V_0 + \frac{1}{2}k_2y^2 + \frac{1}{4!}k_4y^4 + \dots$. The coefficients such as V_0 , k_2 and k_4 can be complicated functions of all the d.c. voltages. The Taylor expansion along x may contain odd terms, such as the x and x^3 terms, and cross terms to y , such as x^2y^2 . However, as we have arranged to trap an electron more tightly along x in its ground state, we can completely ignore x here. Specific to our device configuration shown in Fig. 1 and Extended Data Fig. 1, if the two arms of the resonator-guard electrodes applied with the voltage V_{rg} are indeed perfectly symmetric, then when we slightly tune V_{rg} and keep everything else fixed, the main consequences are the changes of the overall potential minimum V_0 and the linear coefficient along x , but not changes in k_2 or k_4 , and hence they should have a minimal influence on the transition spectrum associated with the electron’s y motion.

However, if the device has some small asymmetries due to fabrication imperfections, a defective solid Ne surface or background electrons in different experiments, then the Taylor expansion of the trapping potential along y must include the linear and cubic terms. At the perturbative level, we can keep just the linear terms, drop the spectrally irrelevant V_0 term and rewrite the potential as

$$V(y) \approx \frac{1}{2}k_2[\beta y + y^2 + \zeta y^4]. \quad (6)$$

The parameter β , with the dimension of length, can be called the asymmetry parameter. The parameter ζ , with the dimension of (length)⁻², can be called the anharmonicity parameter. If $\beta > 0$, the system goes back to a symmetric anharmonic oscillator up to the quartic term. In addition, if $\zeta > 0$ too, the system returns to a simple harmonic oscillator with k_2 as the usual spring constant. All the parameters k_2 , β and ζ are, in principle, functions of the tuning voltage V_{rg} here. However, for small tuning, β is the leading variable whereas k_2 and ζ are approximately constant. At the perturbative level, we can relate β and V_{rg} by $\beta = (V_{rg} - V_{ss})/\eta$, where η is a positive constant and has the physical meaning of a characteristic electric field, and $V_{ss} = 339$ mV is the aforementioned ‘sweet spot’ voltage. If $V_{rg} = V_{ss}$, then $\beta = 0$ and $V(y)$ is symmetric. If $V_{rg} > V_{ss}$, then $\beta > 0$ and $V(y)$ is slightly higher on the right, and so the electron is slightly shifted to the left. If $V_{rg} < V_{ss}$, then $\beta < 0$ and $V(y)$ is slightly higher on the left, and so the electron is slightly shifted to the right. Therefore, the minimal model that can capture most of the experimental features reads

$$V(y) = \frac{1}{2}k_2\left[\frac{V_{rg} - V_{ss}}{\eta}y + y^2 + \zeta y^4\right], \quad (7)$$

Article

where k_2 , η and ζ are all constants to be determined from the experiments. With the choice of $k_2 = 5.536 \text{ meV } \mu\text{m}^{-2}$, $\eta = 0.8271 \text{ V } \mu\text{m}^{-1}$ and $\zeta = 15.4 \text{ } \mu\text{m}^{-2}$, the obtained qubit spectrum and anharmonicity can largely reproduce the experimental results.

Extended Data Figure 8 presents all the calculated qubit properties based on the minimal model above. The trapping potential is flattened at the bottom by the anharmonic quartic term and symmetrically leans to the left and right by tuning V_{rg} with respect to V_{ss} . Electron wavefunctions extend about 500 nm into space and are left and right shifted with the potential changes. In particular, the calculated $|0\rangle \rightarrow |1\rangle$ transition spectrum in Extended Data Fig. 8e is nearly identical to Fig. 3a from the two-tone qubit spectroscopy measurement. The magnified spectrum in the $\pm 100 \text{ MHz}$ detuning range gives the $|1\rangle \rightarrow |2\rangle$ transition with a positive anharmonicity of $\alpha = 40 \text{ MHz}$ at a detuning of -100 MHz , in agreement with Extended Data Fig. 7.

It is known that for a symmetric potential, if only the lowest three energy levels need to be considered, the dispersive shift can be theoretically estimated by $\chi \approx g^2 \alpha / (\Delta + \alpha)$, as is used most often in superconducting transmon qubits. However, for a generally asymmetric potential, the originally forbidden transitions by selection rules are activated and higher-lying levels often need to be included to get an accurate agreement with experiments.

Taking our case as an example, if we assume that the asymmetry is not too drastic and the lowest three levels still dominate the main behaviours, the dispersive shift can be approximated by⁶²

$$\chi = \chi_{01} - \frac{\chi_{12}}{2} + \frac{\chi_{02}}{2}, \quad (8)$$

with contributions from each $i \rightarrow j$ transition (including the previously forbidden $0 \rightarrow 2$ transition),

$$\chi_{ij} = \frac{g_{ij}^2}{\omega_{ij} - \omega_r} = \frac{g_{ij}^2}{\Delta_{ij}}. \quad (9)$$

Here g_{ij} is the generalized coupling strength associated with the $i \rightarrow j$ transition, $\omega_{ij} = \omega_j - \omega_i$ is the transition frequency, ω_r is the resonator frequency and $\Delta_{ij} = \omega_j - \omega_i$ is the generalized detuning. g_{ij} is proportional to the electric dipole strength d_{ij} at the transition frequency and normalized single-photon (zero-point) electric field strength \mathcal{E}_r of the resonator mode.

Further analysis requires calculation of the dipole strengths from the approximate electron wavefunctions obtained from the minimal model above and estimation of the single-photon (zero-point) field strength from the vacuum Rabi splitting measurement. However, we do

not expect that such a simple treatment can lead to a highly meaningful comparison between theory and experiment. We intend to carry out more systematic studies of the single-electron qubit spectroscopy, both experimentally and theoretically, in our future works.

Data availability

The data that support the findings of this study are available from the corresponding authors on request.

Code availability

The computer codes that are used in this study are available from the corresponding authors on request.

Acknowledgements This work was performed at the Center for Nanoscale Materials (CNM), a US Department of Energy Office of Science User Facility, and supported by the US Department of Energy, Office of Science, under Contract no. DE-AC02-06CH11357. D.J. and X.L. acknowledge additional support from Argonne National Laboratory Directed Research and Development (LDRD) Program for device characterization effort. D.J. acknowledges additional support from the Julian Schwinger Foundation (JSF) for Physics Research for hardware component upgrade. This work was partially supported by the University of Chicago Materials Research Science and Engineering Center, which is funded by the National Science Foundation under award no. DMR-2011854. This work made use of the Pritzker Nanofabrication Facility of the Institute for Molecular Engineering at the University of Chicago, which receives support from SHyNE, a node of the National Science Foundations National Nanotechnology Coordinated Infrastructure (NSF NNCI-1542205). D.I.S. and B.D. acknowledge support from NSF grant no. DMR-1906003. K.W.M. acknowledges support from NSF grant no. PHY-1752844 (CAREER) and use of facilities at the Institute of Materials Science and Engineering at Washington University. W.G. acknowledges support from NSF grant no. DMR-2100790 and the National High Magnetic Field Laboratory, which is funded through the NSF Cooperative Agreement no. DMR-1644779 and the State of Florida. G.Y. acknowledges support from the National Science Foundation under Cooperative Agreement no. PHY-2019786 (the NSF AI Institute for Artificial Intelligence and Fundamental Interactions, <http://iaifi.org/>). D.J. thanks M. W. Cole, M. I. Dykman, S. K. Gray, P. Leiderer, D. Lopez and T. Rajh for inspiring discussions. The CNM team thanks MIT Lincoln Laboratory and Intelligence Advanced Research Projects Activity (IARPA) for providing the traveling-wave parametric amplifier (TWPA) used in this project.

Author contributions X. Zhou and D.J. devised the experiment and wrote the manuscript. X. Zhou performed the experiment. G.K., G.Y. and D.I.S. designed the device. G.K. and G.Y. fabricated the device. X. Zhou, X. Zhang, X.H. and D.J. built the experimental setup. B.D. simulated the device. X.L. and R.D. characterized the device. W.G. advised the sample processing and theoretical modelling. K.W.M. and D.I.S. advised the measurement and revised the manuscript. D.J. conceived the idea and led the project. All authors contributed to the manuscript.

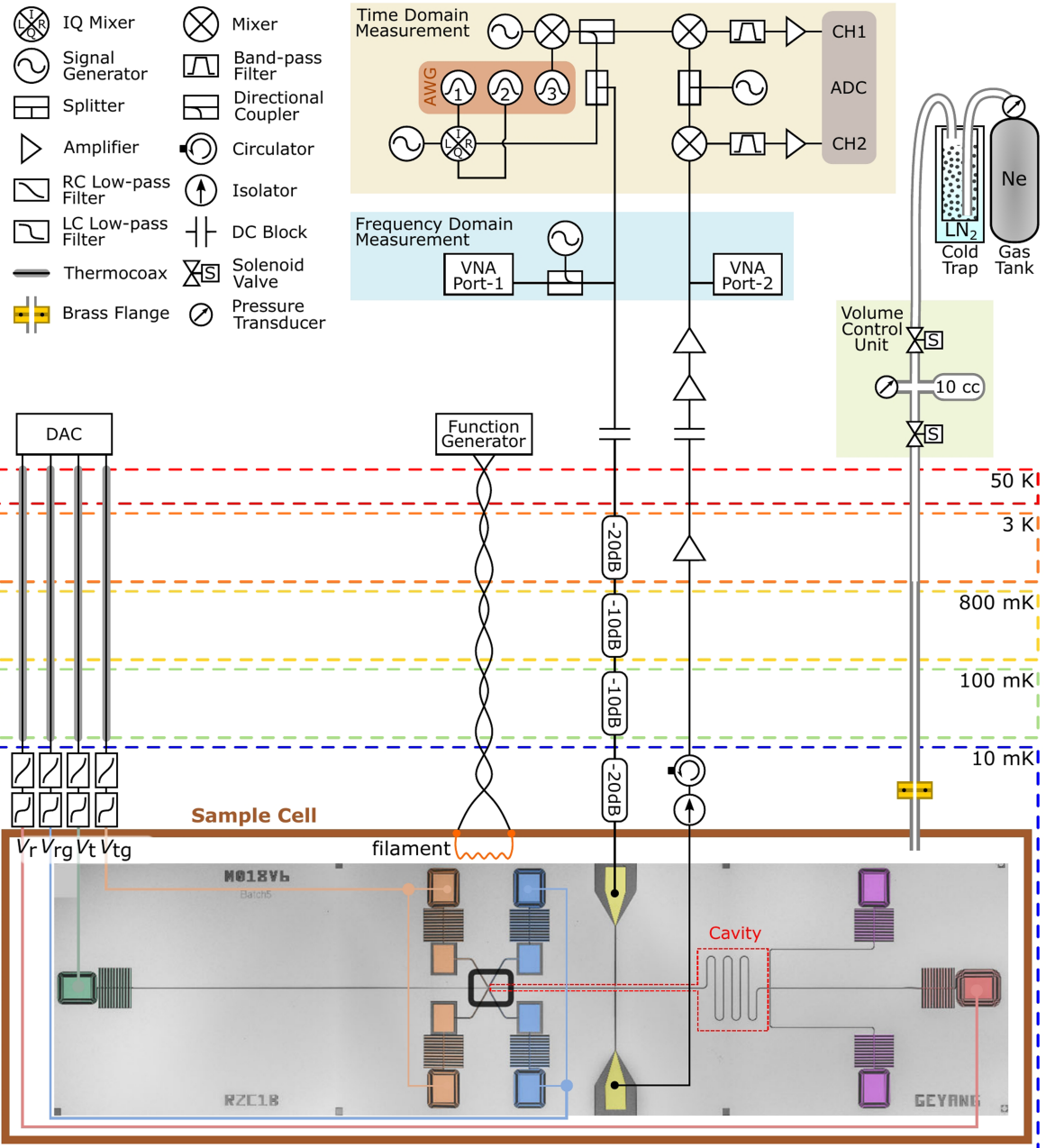
Competing interests Authors declare no competing interests.

Additional information

Correspondence and requests for materials should be addressed to Kater W. Murch or Dafei Jin.

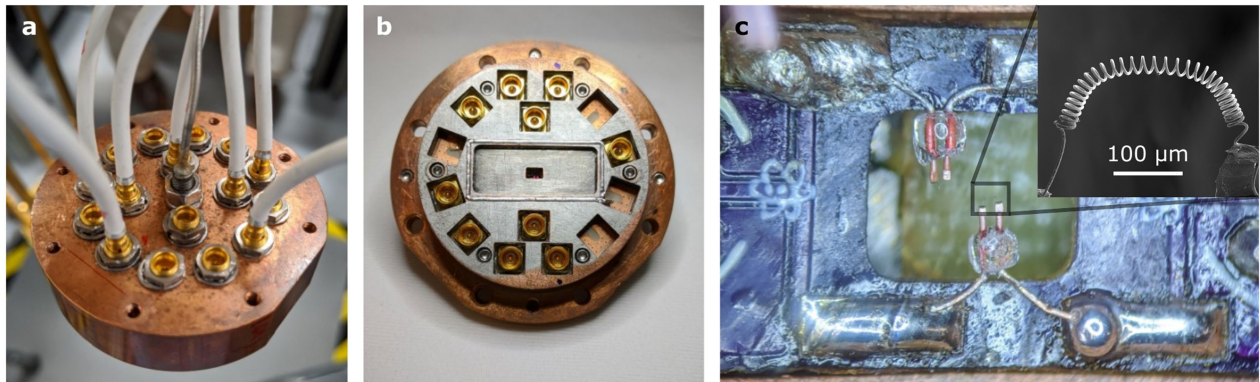
Peer review information *Nature* thanks Mark Dykman, Erika Kawakami and the other, anonymous, reviewer(s) for their contribution to the peer review of this work.

Reprints and permissions information is available at <http://www.nature.com/reprints>.



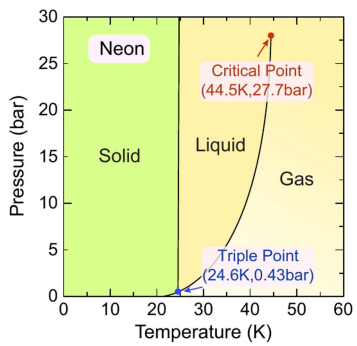
Extended Data Fig. 1 | Cryostat and measurement setup for single-electron qubits on solid neon in a circuit quantum electrodynamics architecture.
Details are explained in the text where they are referred to.

Article



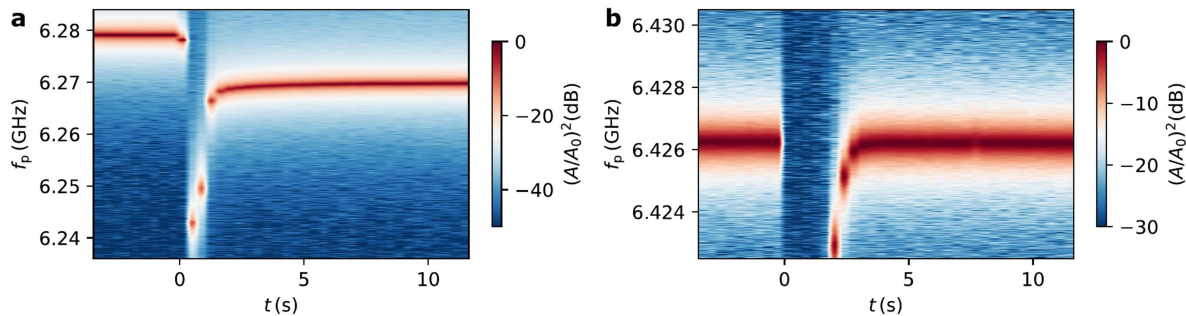
Extended Data Fig. 2 | Photographs of sample cell and electron source. **a**, Lid part of the cell with all the coax connection. It contains 14 hermetic SMP feedthroughs for d.c. and RF signals, 2 SMP feedthroughs for electron source, and a stainless steel tube for neon filling. **b**, Pedestal part of the cell with a printed circuit board (PCB) mounted underneath a stack of copper sheets that

suppress unwanted microwave modes. **c**, Two tungsten filaments, mounted in parallel on the back side of the lid in **(a)**, as the electron source by thermionic emission. The inset shows a scanning electron microscopy (SEM) image of one tungsten filament.



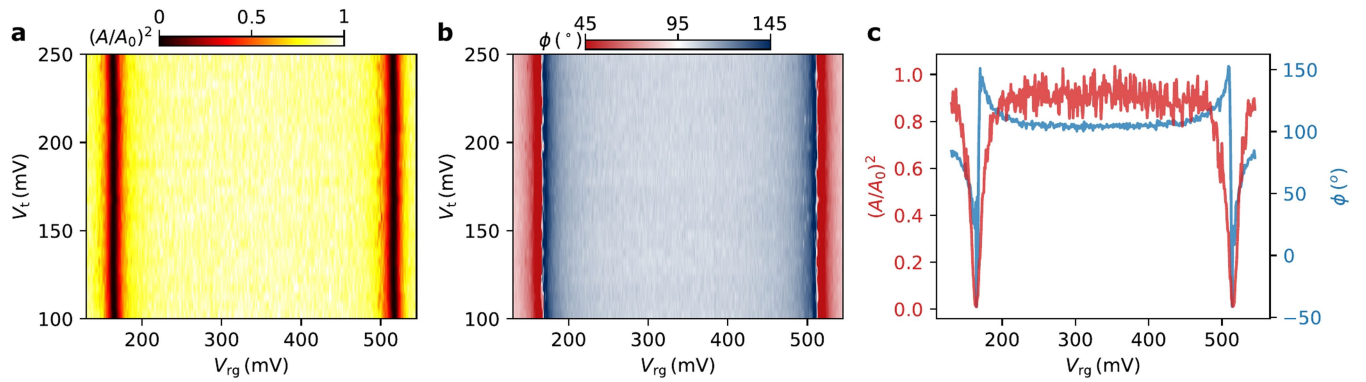
Extended Data Fig. 3 | Phase diagram of neon. The solid-liquid-gas triple point is at (24.56 K, 0.43 bar) and the liquid-gas critical point is at (44.49 K, 27.69 bar).

Article



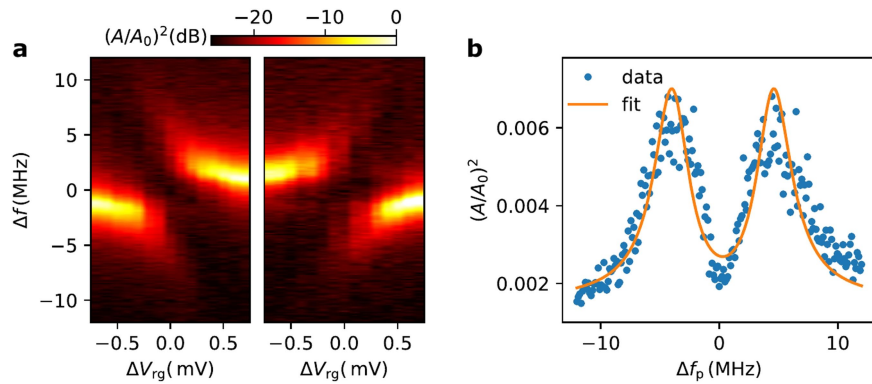
Extended Data Fig. 4 | Observed time evolution of transmission amplitude $(A/A_0)^2$ during the electron generation and deposition processes. **a**, In the case of neon fully filling the channel. **b**, In the case of 5–10 nm neon coating the device. At $t = 0$, pulse train is sent to the tungsten filaments and electrons are

generated and deposited onto the resonator. A sudden change in the spectrum can be seen. After about 3 s, the spectrum stabilizes and shows a frequency shift about 10 MHz for **(a)** and almost no shift for **(b)**.



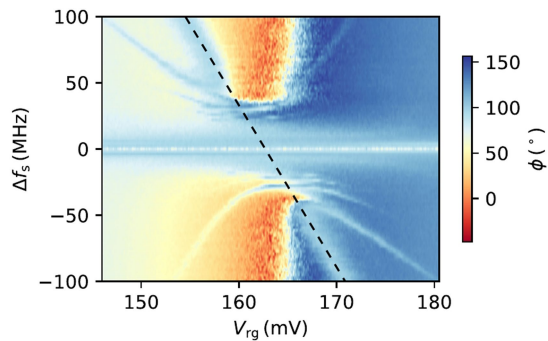
Extended Data Fig. 5 | Coupling of a single electron and microwave photons. **a**, Normalized transmission amplitude $(A/A_0)^2$ probed at the bare resonator frequency f_r as a function of the resonator-guard voltage V_{rg} and the trap voltage V_t . **b**, Transmission phase ϕ , corresponding to the amplitude in (a),

as a function of V_{rg} and V_t . **c**, Line scanned normalized amplitude $(A/A_0)^2$ and phase ϕ as a function of V_{rg} at $V_t = 175$ mV. A dip in amplitude and 2π phase jump occur when the qubit frequency matches the resonator frequency.



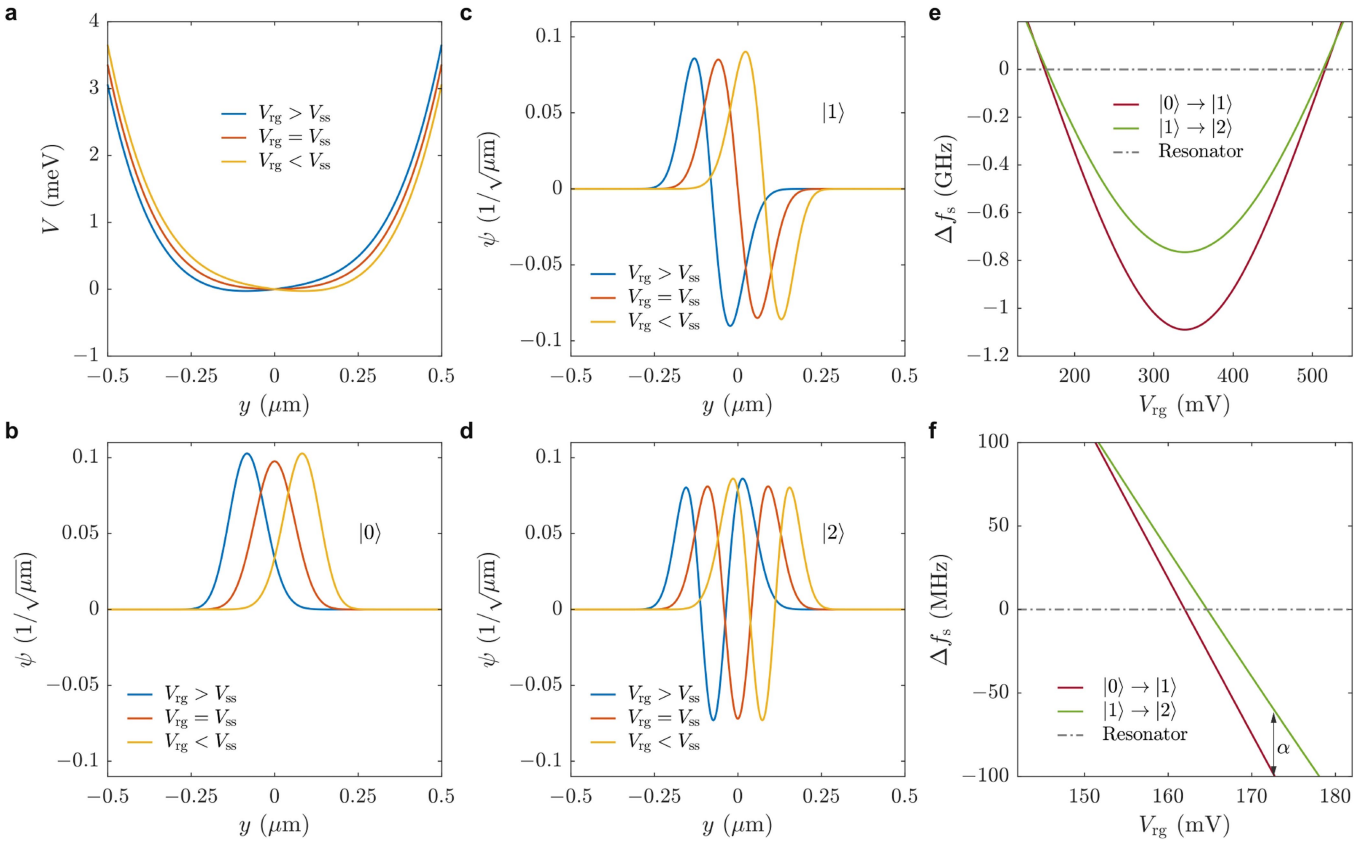
Extended Data Fig. 6 | Vacuum Rabi splitting between a single electron and microwave photons. **a**, Normalized transmission amplitude $(A/A_0)^2$ as a function of probe frequency $\Delta f_p = f_p - f_r$ and resonator-guard voltage ΔV_{rg} (detuning from the resonance condition). **b**, Transmission amplitude $(A/A_0)^2$

versus a probe frequency when qubit and resonator is on resonance. The fitting curve with input-output theory gives a coupling strength $g/2\pi$ about 4.5 MHz and qubit decay rate $\gamma/2\pi$ about 3.4 MHz.



Extended Data Fig. 7 | Two-tone qubit spectroscopy measurement with high pump power and pump frequency around the bare resonator frequency.

Besides the $|0\rangle \rightarrow |1\rangle$ transition line, which is marked with black dashed line, there are other transition lines visible. The line immediately next to the main transition line is the $|1\rangle \rightarrow |2\rangle$ transition. At $\Delta/2\pi = f_q - f_r = -100$ MHz detuning, the anharmonicity $\alpha/2\pi \equiv f_{|1\rangle \rightarrow |2\rangle} - f_{|0\rangle \rightarrow |1\rangle} \approx 40$ MHz.



Extended Data Fig. 8 | Calculated electron qubit properties based on a minimal model that encloses linear asymmetry and quartic anharmonicity. **a**, Trapping potential V versus position y . The shape symmetrically leans to the left and right by tuning the resonator-guard voltage V_{rg} with respect to the ‘sweet spot’ voltage $V_{\text{ss}} = 339$ mV. For $V_{\text{rg}} > V_{\text{ss}}$, we take $V_{\text{rg}} = 516$ mV and for $V_{\text{rg}} > V_{\text{ss}}$, we take $V_{\text{rg}} = 162$ mV, both of which are on-resonance conditions in experiment when the qubit frequency f_q matches the resonator frequency f_r . **b–d**, Electron wavefunctions on the ground state $|0\rangle$, first excited state $|1\rangle$, and second excited state $|2\rangle$, respectively, for the three different V_{rg} ’s. They extend about 500 nm in

space and are left and right shifted with the potential changes. **e**, Qubit spectrum under frequency scanning $\Delta f_s = f_s - f_r$ and voltage V_{rg} detuning, for $|0\rangle \rightarrow |1\rangle$ and $|1\rangle \rightarrow |2\rangle$ transitions. The first transition (in red) matches well with the experimental observation shown in Fig. 3a. **f**, Magnified qubit spectrum of (e) in the ± 100 MHz detuning range. The second transition has a positive anharmonicity $\alpha = 40$ MHz above the first transition at -100 MHz detuning. The overall spectral profile also matches the experiment observation shown in Extended Data Fig. 7, taking account of the practical spectrum deformation due to the overly strong pumping near resonance.